Applied Physics Letters

RESEARCH ARTICLE | OCTOBER 22 2025

Low-loss GaN monolithic bidirectional switch via antiparallel connected HEMTs with recessed Schottky drain

Yi Ma; Yudong Li; Xuanling Zhou; Han Gao; Yitai Zhu; Haolan Qu ; Kerui Li ; Hongzhi Wang ; Xinbo Zou

Check for updates

Appl. Phys. Lett. 127, 163305 (2025)
https://doi.org/10.1063/5.0292563

View Online
Export Citation

Articles You May Be Interested In

Development of process parameters for 22 nm PMOS using 2-D analytical modeling

AIP Conf. Proc. (April 2015)

A model of antiparallel spontaneous and piezoelectric polarizations in AlGaN/GaN

AIP Conf. Proc. (July 2019)

An asymptotic theory for the nonlinear instability of antiparallel pairs of vortex filaments

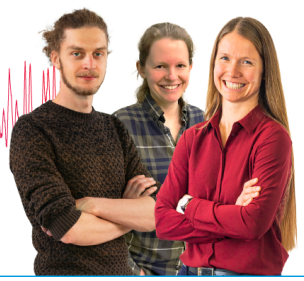
Phys. Fluids (February 1993)

03 November 2025 04:02:20

Webinar From Noise to Knowledge

May 13th – Register now

Zurich Instruments
Universität Konstanz



AIP Publishing

Applied Physics Letters ARTICLE pubs.aip.org/aip/apl

Low-loss GaN monolithic bidirectional switch via antiparallel connected HEMTs with recessed Schottky drain

Cite as: Appl. Phys. Lett. **127**, 163305 (2025); doi: 10.1063/5.0292563
Submitted: 23 July 2025 · Accepted: 1 October 2025 ·
Published Online: 22 October 2025

View Online Export Citation CrossMark

Yi Ma,[1] Yudong Li,[1] Xuanling Zhou,[1] Han Gao,[1] Yitai Zhu,[1] Haolan Qu,[1] Kerui Li,[2] Hongzhi Wang,[2] and Xinbo Zou[1,a)]

AFFILIATIONS

[1]School of Information Science and Technology, ShanghaiTech University, Shanghai 201210, People's Republic of China
[2]College of Materials Science and Engineering, Donghua University, Shanghai 201620, People's Republic of China

[a)]Author to whom correspondence should be addressed: zouxb@shanghaitech.edu.cn

ABSTRACT

A low-loss gallium nitride monolithic bidirectional switch (MBDS) is demonstrated by antiparallel connecting two high electron mobility transistors (HEMTs), which feature recessed Schottky-type drain and reverse blocking (RB) property. The RB-HEMT shows a low turn-on voltage (V_{ON}) of 0.33 V and a reverse leakage current (I_{LEAK}) of 300 nA/mm. Moreover, the MBDS exhibits outstanding static performance with a low specific ON-resistance ($R_{ON,SP}$) of 1.18 m$\Omega \cdot cm^2$, a high saturated current density (I_{sat}) of 380 mA/mm, a breakdown voltage of 425 V, and a high Baliga's figure of merit of 153 MW/cm^2. In addition, the MBDS shows highly efficient pulse width modulation as an AC chopper and low switching loss. These results highlight the promise of the proposed MBDS for power conversion applications.

Published under an exclusive license by AIP Publishing. https://doi.org/10.1063/5.0292563

03 November 2025 04:02:20

The monolithic bidirectional switch (MBDS), capable of sustaining high voltage in the off-state and conducting current in both directions, features high energy efficiency and compact device configuration, making it attractive for power applications such as grid interfaces, motor drives, and battery management systems.[1,2] Lateral MBDSs based on gallium nitride (GaN) high electron mobility transistors (GaN HEMTs) have attracted extensive research interest compared with devices made of silicon carbide (SiC)[3] and gallium oxide (Ga_2O_3),[4,5] owing to their outstanding high frequency performance, low conduction loss, and ease of integration.[6–8] Dual gate and diode bridge configurations are among the typical approaches to realizing GaN MBDSs.[9,10] The dual gate MBDS features a shared drift region to enable bidirectional current conduction and to achieve chip area reduction. However, in the diode mode of dual gate MBDS, where one gate turns on and the other turns off, the device shows increased ON-resistance (R_{ON}) and higher turn-on voltage (V_{ON}) than that in the bidirectional conducting mode, as the drain voltage needs to forward bias the off-state gate junction.[6,11] The diode bridge MBDS, which integrates four Schottky barrier diodes (SBDs) and one HEMT, simplifies gate driving but suffers from a high V_{ON} due to the forward voltage drop across two series-connected SBDs.[9,12] MBDS can also be realized using two antiparallel connected reverse blocking HEMTs (RB-HEMTs). This configuration achieves low V_{ON} and stable R_{ON} across different gate driving conditions, making it preferable for matrix converters employing two-step current-direction-based commutation.[13,14]

As a unit cell of the MBDS, the RB-HEMT, which typically involves a Schottky-type drain to enable forward conduction and reverse blocking, has been extensively investigated to improve V_{ON}, R_{ON}, and reverse leakage current (I_{LEAK}). Wu *et al.* proposed an RB-HEMT with Al_2O_3 dielectric to achieve a low V_{ON} of ∼1 V and an R_{ON} of ∼41.7 $\Omega \cdot$ mm.[15] The V_{ON} and R_{ON} can be lowered by reducing the barrier layer thickness in the drain terminal, thereby lowering the conduction loss. Toward a recessed-drain, Cl_2/BCl_3-based inductively coupled plasma reactive ion etching (ICP-RIE) has been commonly used for AlGaN layer etching. For example, Wang *et al.* investigated a drain-recessed RB-HEMT via ICP-RIE to achieve a V_{ON} of ∼0.63 V and an R_{ON} of ∼28.5 $\Omega \cdot$ mm.[16] However, the associated ion bombardment and ultraviolet photon exposure during the ICP-RIE process inevitably induce etching damage in the recessed region, thereby degrading the V_{ON}, R_{ON}, and I_{LEAK}. Lei *et al.* have employed plasma oxidation and hydrogen chloride treatment in the recessed region to reduce etching damage, achieving a lower V_{ON} of ∼0.5 V, an R_{ON} of ∼11 $\Omega \cdot$ mm, and an I_{LEAK} of ∼20 nA/mm.[14] Wang *et al.* managed to mitigate etching damage by annealing at 450 °C with nitrogen,

Published under an exclusive license by AIP Publishing

achieving a low V_{ON} of ~0.25 V and an R_{ON} of ~10.4 Ω · mm. However, the etching damage was not fully eliminated, as evidenced by an I_{LEAK} of ~2 μA/mm.[17] Recently, neutral beam etching (NBE) has garnered extensive research interest in achieving low-damage and precise material removal. This technique employs neutralized ions to achieve etching while preventing charge accumulation and radiation-induced defects.[18–20] In this work, an argon-based NBE process was employed to selectively etch the AlGaN barrier layer, enabling the fabrication of RB-HEMT with a Schottky-type drain that exhibits low V_{ON} and I_{LEAK}. Moreover, MBDS was constructed by antiparallel connecting two RB-HEMTs, demonstrating excellent static and dynamic performance with low conduction and switching losses.

Figure 1(a) illustrates the device structure and equivalent circuit of the RB-HEMT, in which the drain is recessed and formed with a Schottky contact. The GaN-based epilayers were grown on a 6-inch silicon substrate by metal organic chemical vapor deposition (MOCVD). The epitaxial structure consists of a 23 nm $Al_{0.26}Ga_{0.74}N$ barrier layer, a 0.8 nm AlN spacer layer, a 210 nm i-GaN layer, and a 5 μm undoped-GaN buffer layer. The Hall effect measurement showed a sheet resistance of ~280 Ω/square and an electron mobility of ~1900 $cm^2/V \cdot s$. The fabricated RB-HEMT device can be regarded as an HEMT connected in series with an SBD. As shown in Fig. 1(b), two RB-HEMTs are connected in an antiparallel configuration to construct the MBDS, where the drain of one RB-HEMT is linked to the source of the other transistor via a metal pad, defined as Source1 (S1) and Source2 (S2). The fabrication process starts from mesa isolation, followed by Ti/Al/Ni/Au (20/150/50/80 nm) ohmic contacts deposition and rapid thermal annealing at 850 °C for 40 s in an N_2 ambient. The recessed region was achieved through the NBE process using 200 eV argon-based plasma for 340 s, achieving an etching depth of 17.2 nm. A 15 nm Al_2O_3 layer was deposited by plasma enhanced atomic layer deposition (PEALD) at 300 °C, serving as the gate dielectric and surface passivation. Finally, the Al_2O_3 layer in the recessed regions was removed by HF/NH_4F solution for 2 min. Ni/Au (20/200 nm) was deposited on the gate electrodes, the recessed regions of S1 and S2, and the ohmic contacts to serve as pad interconnections. Figure 1(c) is a scanning electron microscope (SEM) image of the fabricated MBDS, and the measured device dimensions are shown in the zoomed-in SEM image in Fig. 1(d), featuring $L_{G1} = L_{G2} = 2.5$ μm, $L_{G1S1} = L_{G2S2} = 1.5$ μm, $L_{G1S2} = L_{G2S1} = 4.4$ μm, and $W_G = 23.6$ μm, respectively.

As shown in Fig. 2(a), the RB-HEMT can sustain reverse voltage when V_{GS} exceeds the threshold voltage (V_{TH}), which differs from

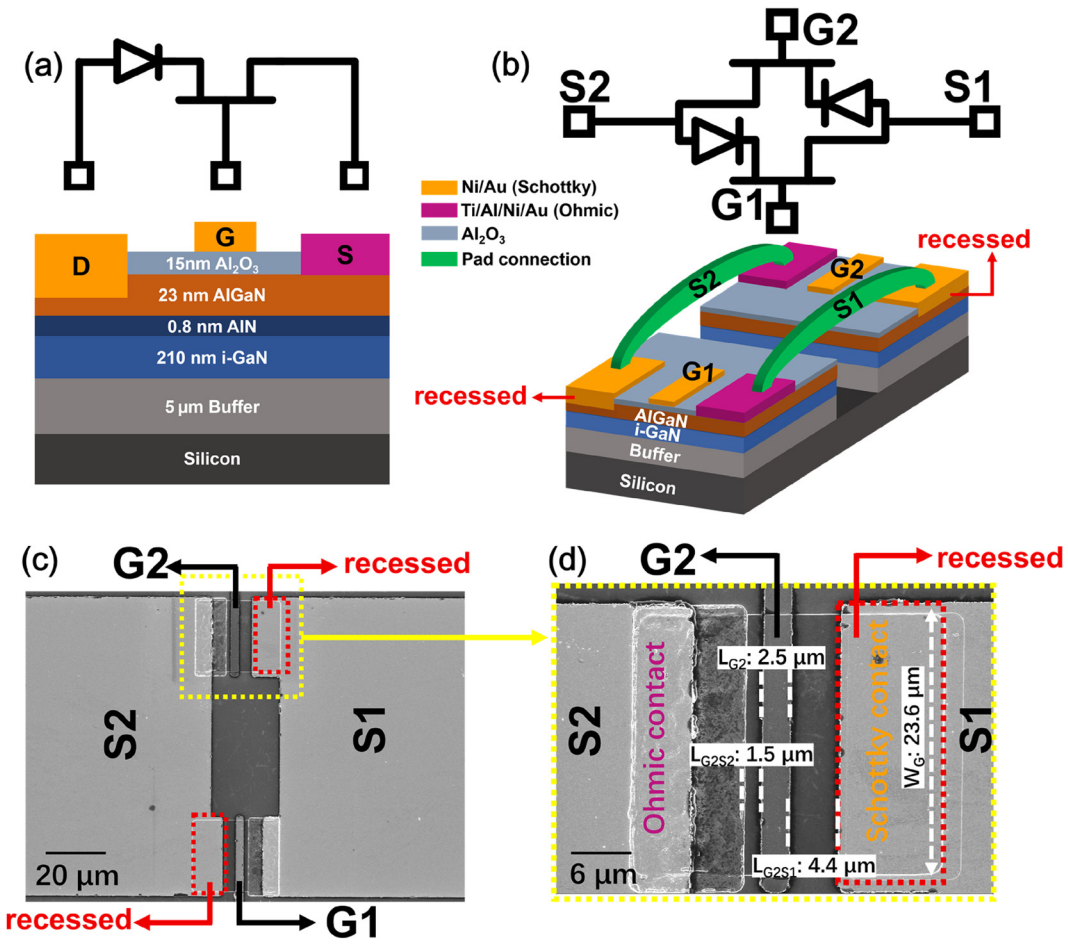


FIG. 1. (a) The schematic of the RB-HEMT, (b) the schematic of the MBDS, (c) SEM image of the MBDS, and (d) zoomed-in image of (c) with device dimensions.

03 November 2025 04:02:20

Published under an exclusive license by AIP Publishing

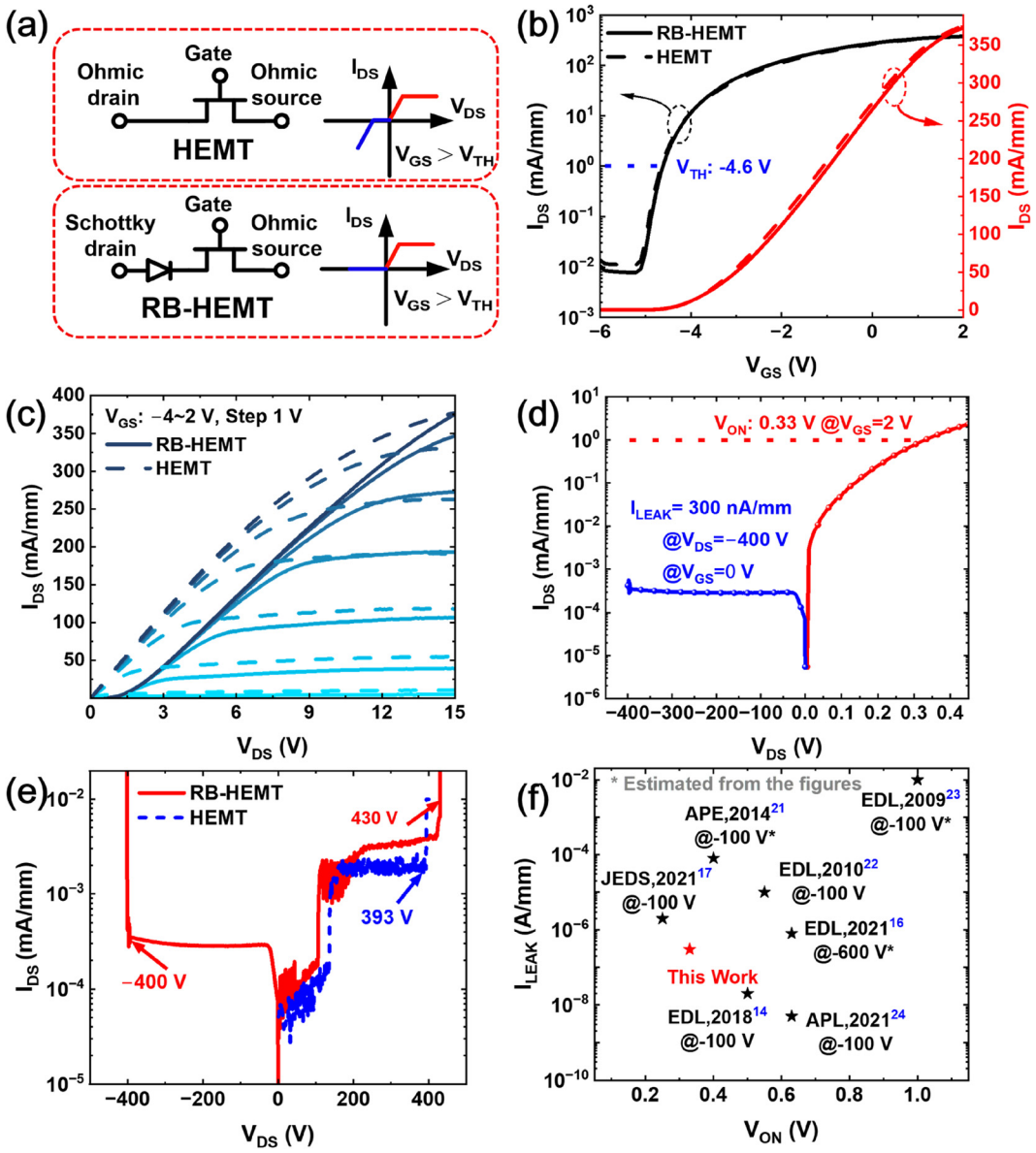


FIG. 2. (a) Equivalent schematics of the HEMT and RB-HEMT, (b) transfer characteristics, (c) forward output characteristics, (d) log-scaled output characteristics, (e) breakdown characteristics, and (f) benchmark of drain-recessed RB-HEMTs.

HEMT with ohmic-type drain. Figure 2(b) presents the transfer characteristics of the RB-HEMT and HEMT, which exhibit an identical V_{TH} of −4.6 V at I_{DS} = 1 mA/mm. As shown in Fig. 2(c), the R_{ON} of ∼9.7 Ω · mm (∼13 Ω · mm) for HEMT (RB-HEMT) is calculated by the reciprocal of output conductance. Figure 2(d) shows the log-scaled output characteristics, where the I_{LEAK} is ∼300 nA/mm when V_{DS} = −400 V and V_{GS} = 0 V, demonstrating an outstanding reverse blocking capability. The V_{ON} of ∼0.33 V is achieved at I_{DS} = 1 mA/mm, which is primarily determined by the Schottky barrier height at the recessed region. Figure 2(e) shows the breakdown voltages of the RB-HEMT and HEMT devices, which are measured when drain leakage current reaches 10 μA/mm with a floating substrate. The red solid curve represents the forward and reverse breakdown voltages of the RB-HEMT, while the blue dashed curve corresponds to the forward breakdown voltage of the HEMT. The RB-HEMT can not only sustain a forward voltage of ∼430 V at V_{GS} = −10 V but also sustain a reverse voltage of ∼400 V at V_{GS} = 0 V. However, the HEMT only sustains a forward voltage of ∼394 V at V_{GS} = −10 V. Figure 2(f) compares the V_{ON} vs I_{LEAK} characteristics of the proposed drain-recessed RB-HEMT.[21–23] In the literature,[14,24] a higher AlGaN barrier height near the drain effectively suppresses reverse leakage current by reducing electron tunneling, but at the cost of a higher V_{ON}. In contrast, the

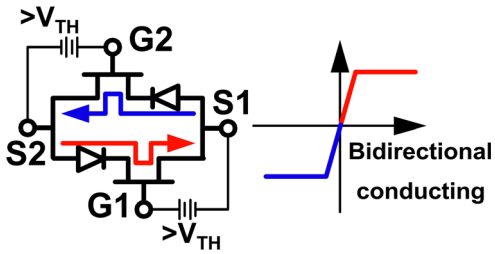
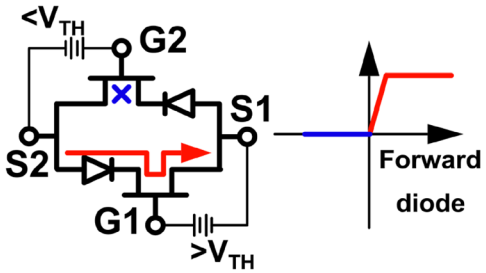
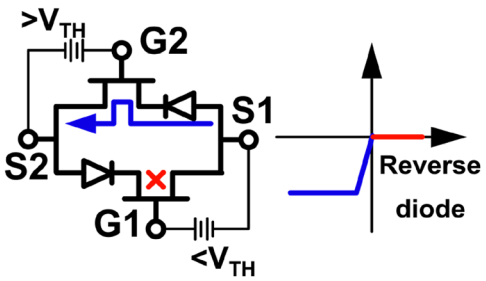
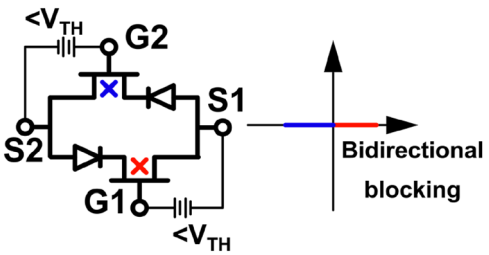
03 November 2025 04:02:20

Published under an exclusive license by AIP Publishing

realization of an ohmic–Schottky hybrid drain helps reduce V_{ON} but introduces an additional current leakage path, resulting in higher I_{LEAK}, as reported in the literature.[17]

The operating principle of the proposed MBDS is illustrated in Table I, including four operating modes: bidirectional conducting/blocking modes and forward/reverse diode modes. As $V_{G1S1} > V_{TH}$ and $V_{G2S2} > V_{TH}$, the MBDS operates in a bidirectional conducting mode, allowing current conduction in both forward and reverse directions. As $V_{G1S1} > V_{TH}$ and $V_{G2S2} < V_{TH}$ (or $V_{G1S1} < V_{TH}$ and $V_{G2S2} > V_{TH}$), the MBDS operates in the forward (or reverse) diode mode, conducting forward current and sustaining reverse voltage (or conducting reverse current and sustaining forward voltage). When $V_{G1S1} < V_{TH}$ and $V_{G2S2} < V_{TH}$, the MBDS operates in bidirectional blocking mode and is capable of sustaining voltage in both directions. The current–voltage characteristics of the MBDS are measured using a semiconductor analyzer with three source-measure units and a ground unit as illustrated in Fig. 3(a). During the measurement of the bidirectional conducting mode, S1 is grounded, while S2 is swept with G2 synchronized to maintain $V_{G1S1} = V_{G2S2}$. Figure 3(b) shows the bidirectional output characteristics of the MBDS, where V_{G1S1} and V_{G2S2} are swept simultaneously from −4 to 2 V with a step of 1 V. The I_{sat} is ∼380 mA/mm in both directions when both gates are biased at 2 V, and the forward (reverse) R_{ON} is ∼14 Ω · mm (∼18 Ω · mm), respectively. The slight R_{ON} asymmetry is attributed to immature fabrication

TABLE I. Four operating modes of the MBDS.

Mode	V_{G1S1}	V_{G2S2}	Schematic
Bidirectional conducting	$>V_{TH}$	$>V_{TH}$	
Forward diode	$>V_{TH}$	$<V_{TH}$	
Reverse diode	$<V_{TH}$	$>V_{TH}$	
Bidirectional blocking	$<V_{TH}$	$<V_{TH}$	

03 November 2025 04:02:20

Published under an exclusive license by AIP Publishing

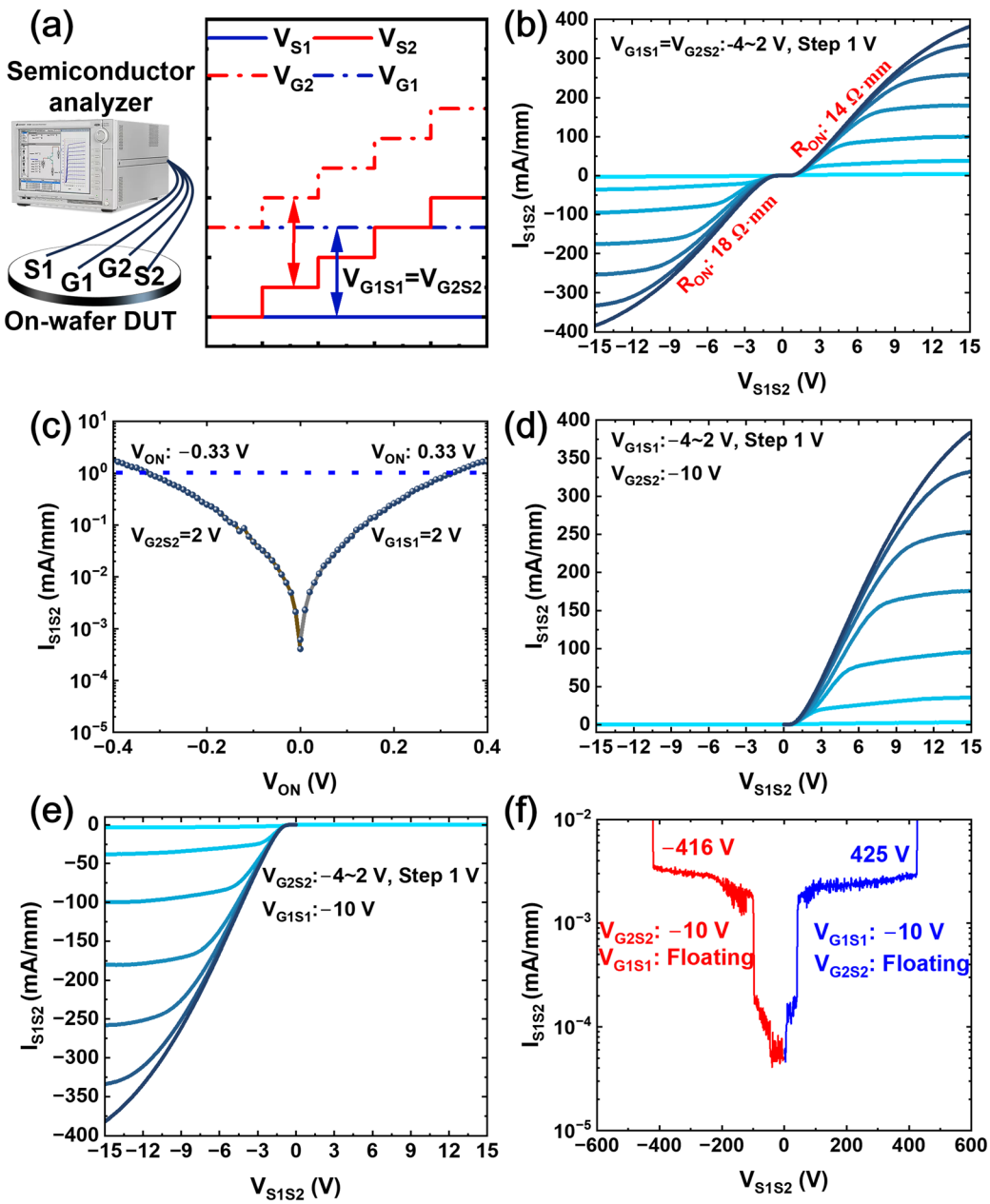


FIG. 3. (a) Schematic of MBDS experiment setup, (b) output characteristics of the bidirectional conducting mode, (c) log-scaled output characteristics of the bidirectional conducting mode. (d), (e) output characteristics in the forward and reverse diode mode, and (f) bidirectional breakdown voltages.

processes such as misalignment and over-development during photolithography, which can be mitigated by the precise alignment and optimizing reaction time during development. Figure 3(c) shows a symmetrical V_{ON} of ~0.33 V (−0.33 V) in the forward (reverse) direction, consistent with the RB-HEMT in Fig. 2(d). Figure 3(d) presents the output characteristics operating in the forward diode mode, where V_{G2S2} is biased at −10 V, and the V_{G1S1} is swept from −4 to 2 V. A similar result is observed when V_{G1S1} is biased at −10 V and V_{G2S2} is swept from −4 to 2 V, as shown in Fig. 3(e). Compared with Figs. 3(b), 3(d), and 3(e), the forward diode mode and reverse diode mode show no significant degradation in R_{ON} and V_{ON} during conduction. In contrast, the dual gate MBDS shows the higher R_{ON} and V_{ON} in the forward diode mode compared with the bidirectional conducting mode.[6] In the dual gate MBDS, bidirectional conduction occurs through a shared path. In the forward diode mode, turning off one gate forces the electrons to traverse a reverse-biased junction, thus

03 November 2025 04:02:20

Published under an exclusive license by AIP Publishing

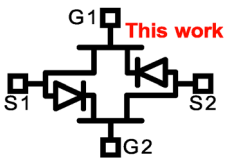
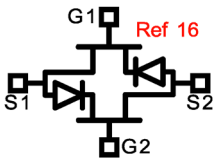
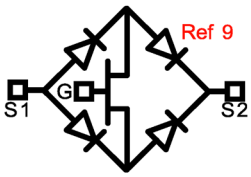
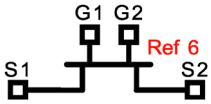
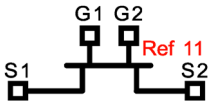
requiring a high V_{S1S2} to overcome the barrier.[11] Figure 3(f) shows the bidirectional breakdown voltages of the MBDS. With $V_{G1S1} = -10$ V and V_{G2S2} floating, a forward breakdown voltage of ~425 V is achieved when I_{S1S2} reaches 10 μA/mm. Conversely, with $V_{G2S2} = -10$ V and V_{G1S1} floating, the reverse breakdown voltage reaches ~416 V. The specific R_{ON} ($R_{ON,SP}$) is ~1.18 (1.51) mΩ · cm^2, and Baliga's figure of merit (FOM) is ~153 (115) MW/cm^2 calculated by $BV^2/R_{ON,SP}$ in the forward (reverse) direction, respectively, where BV is the breakdown voltage. Table II summarizes the key metrics of the fabricated MBDS in comparison with previously reported MBDS structures. A diode bridge MBDS with a high breakdown voltage (~1115 V, $L_{GD} = 22$ μm) was reported; however, a high V_{ON} of ~1.13 V and a low I_{sat} of ~140 mA/mm were observed.[9] Similarly, a dual gate MBDS achieved zero V_{ON} in the bidirectional conducting mode; however, a large V_{ON} of ~3 V was observed in the diode model, along with a low I_{sat} of ~130 mA/mm.[11] Additionally, an MBDS consisting of two antiparallel connected RB-HEMTs with fully recessed Schottky drains was reported.[16] It showed a V_{ON} of ~0.63 V, an $R_{ON,SP}$ of ~6.6 mΩ · cm^2, an I_{sat} of ~225 mA/mm, and an FOM of 66.8 MW/cm^2. In contrast, the MBDS in this work is fabricated using a low-damage NBE process, which effectively eliminates plasma-induced surface degradation and results in significantly improved device performance, showing a low V_{ON} of ~0.33 V, a low $R_{ON,SP}$ of ~1.18 mΩ · cm^2, a high FOM of ~153 MW/cm^2, and a high I_{sat} of ~380 mA/mm.

The AC chopper circuit, in which the output voltage is modulated by varying the duty cycle of the gate driving signal, is demonstrated using the fabricated MBDS.[25] Figure 4(a) shows that a 20 Hz sinusoidal AC signal with a peak amplitude of 10 V is applied to the circuit, while the gate is driven by a 1 kHz square wave with a voltage swing from −5 to 0 V. The duty cycle of the square wave varies from 10% to 90% to evaluate its effect on the output waveform. A typical output waveform obtained at a 50% duty cycle is shown in Fig. 4(b). Although a slight amplitude distortion is observed, the output waveform remains a sinusoidal shape. Figure 4(c) illustrates the frequency spectrum of the output waveform with varying duty cycles. The spectrum exhibits a dominant second harmonic component, while higher-order harmonics are substantially suppressed. Additionally, as the duty cycle increases, the amplitude of the fundamental component (20 Hz) decreases significantly, indicating that the output voltage can be effectively modulated through pulse width control. The total harmonic distortion is demonstrated by

$$\text{Total harmonic distortion} = \frac{\sqrt{V_2^2 + V_3^2 + V_4^2 + V_5^2}}{V_1} \times 100\%, \quad (1)$$

where V_N is the amplitude of the Nth content. As shown in Fig. 4(d), the total harmonic distortion increases from 50.2% to 59.7% with the increasing duty cycle. These results underscore the importance of duty cycle optimization in chopper circuits for improving waveform quality and conversion efficiency. Additionally, the turn-off performance of

TABLE II. Comparison of state-of-the-art GaN-based MBDS devices. The bold values in Table II denote the results from our work and are emphasized for clear comparison.

Configuration	V_{ON} (V)[a]	$R_{ON,SP}$ (mΩ·cm^2)	BV/L_{GD} (V/μm)	I_{sat} (mA/mm)
	**0.33/0.33**	**1.18**	**425/4.4 @10 μA/mm**	**380**
	0.63/0.63	6.6[b]	664/15 @1 μA/mm	225
	1.13/1.13	···	1115/22 @1 mA/mm	140
	0/1.6	5.6	3300/19 @1 μA/mm	250[b]
	0/3	3.3[b]	650/22 @1 nA/mm	130[b]

[a]The V_{ON} is extracted in the bidirectional conducting mode/forward diode mode.
[b]Estimated from the figures.

03 November 2025 04:02:20

Published under an exclusive license by AIP Publishing

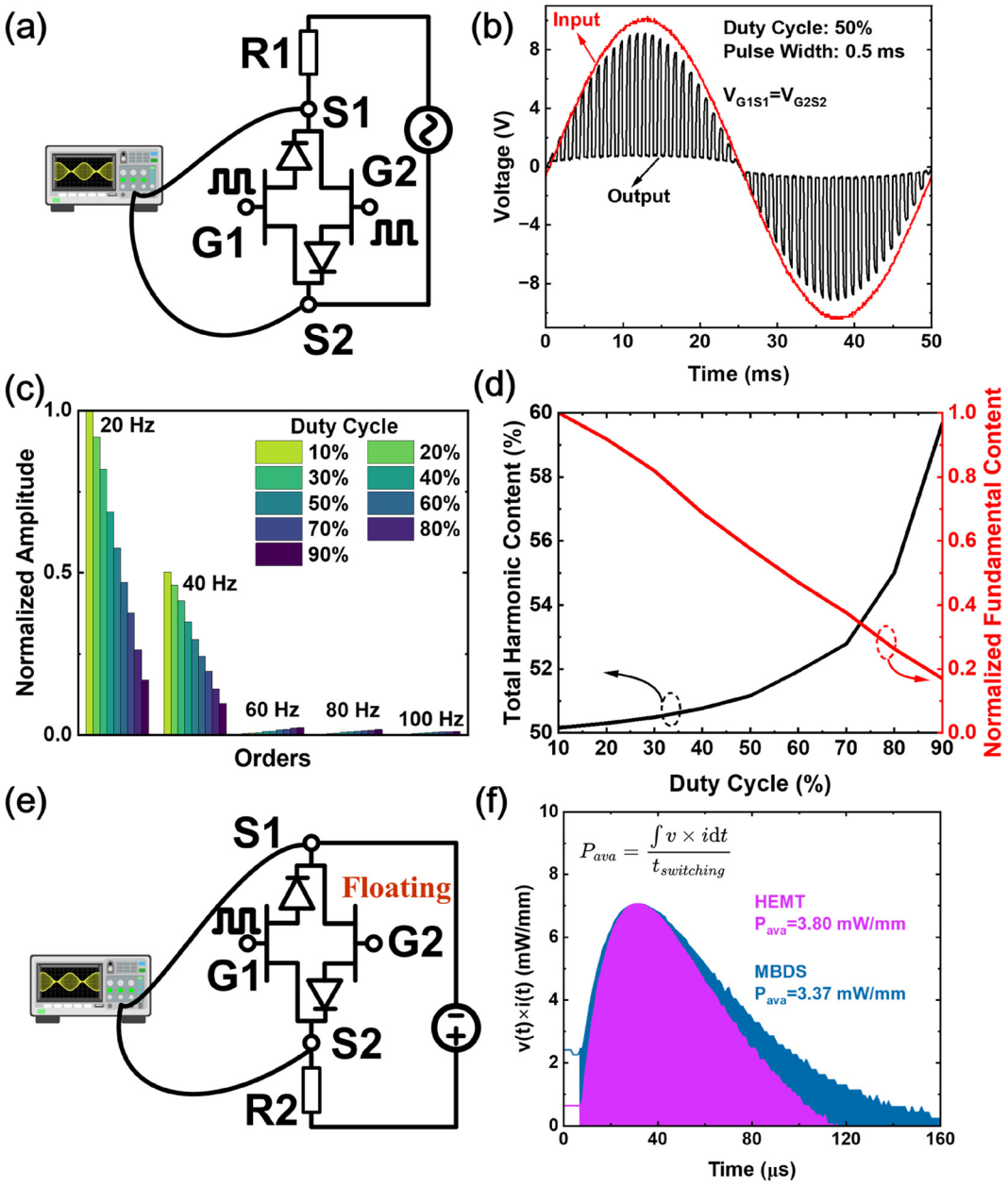


FIG. 4. (a) Test circuit schematic of the AC chopper, (b) AC chopper output waveform with 50% duty cycle, (c) spectrum decomposition of output waveforms under different duty cycles, (d) total harmonic distortion variation with duty cycles, and (f) average power loss density comparison between the MBDS and HEMT.

the MBDS and the conventional HEMT are evaluated under identical experimental conditions. In Fig. 4(e), one gate of the MBDS is driven by a 1 kHz, −5 V to 0 V square wave with a 50% duty cycle, whereas the other gate is floating. Figure 4(f) shows that the MBDS achieves an average switching power loss density of ∼3.37 mW/mm (switching energy loss of ∼6.13 mJ/cm^2), compared with ∼3.80 mW/mm of the HEMT. Compared with vertical SiC MBDS, the proposed GaN MBDS exhibits a lower switching energy loss of ∼6.13 mJ/cm^2, in contrast to ∼12 mJ/cm^2 of the SiC MBDS.[26] Compared with vertical insulated-gate bipolar transistor (IGBT) MBDS,[27] the GaN MBDS in this work shows a higher switching energy loss of ∼6.13 mJ/cm^2 relative to ∼1.7 mJ/cm^2 of the IGBT MBDS. Nevertheless, the $R_{ON,SP}$ of IGBT MBDS (∼140 mΩ · cm^2) is over two orders of magnitude larger than that of the GaN MBDS (∼1.18 mΩ · cm^2), underscoring the superior conduction performance of GaN MBDS in this work.

In this study, a low-loss GaN-based MBDS was experimentally demonstrated by antiparallel connecting two RB-HEMTs. Each RB-HEMT employed a recessed Schottky drain by the low-damage neutral

03 November 2025 04:02:20

Published under an exclusive license by AIP Publishing

beam etching (NBE) process, achieving a low V_{ON} of ~0.33 V and an I_{LEAK} of ~300 nA/mm. Additionally, the MBDS exhibited excellent static performance with a low $R_{ON,SP}$ of ~1.18 mΩ · cm^2, a high I_{sat} of ~380 mA/mm, a breakdown voltage of ~425 V, and a high Baliga's FOM of ~153 MW/cm^2. It also showed a highly efficient pulse width modulation as an AC power chopper and lower switching loss than conventional GaN HEMT under identical conditions. These results highlight the potential of the MBDS for high-efficiency power conversion applications.

This work was supported by the National Natural Science Foundation of China (Grant No. 52131303). The authors would like to thank ShanghaiTech Material and Device Lab (SMDL) for technical support.

AUTHOR DECLARATIONS

Conflict of Interest

The authors have no conflicts to disclose.

Author Contributions

Yi Ma: Conceptualization (lead); Funding acquisition (lead); Investigation (lead); Project administration (lead); Supervision (lead); Writing – original draft (lead); Writing – review & editing (lead). **Yudong Li:** Conceptualization (lead); Investigation (lead); Resources (equal); Writing – original draft (lead). **Xuanling Zhou:** Resources (equal). **Han Gao:** Resources (equal). **Yitai Zhu:** Resources (equal); Validation (equal). **Haolan Qu:** Writing – review & editing (equal). **Kerui Li:** Writing – review & editing (equal). **Hongzhi Wang:** Writing – review & editing (equal). **Xinbo Zou:** Conceptualization (equal); Funding acquisition (lead); Project administration (lead); Supervision (lead); Writing – review & editing (lead).

DATA AVAILABILITY

The data that support the findings of this study are available from the corresponding author upon reasonable request.

REFERENCES

[1]J. W. Kim, B. Kim, D. Lee, Y. Cho, S. K. Ji, and D. Ryu, IEEE Trans. Transp. Electrif. **10**(4), 10169 (2024).
[2]J. Huber and J. W. Kolar, IEEE Power Electron. Mag. **10**(1), 28 (2023).
[3]K. Han, A. Agarwal, A. Kanale, B. J. Baliga, S. Bhattacharya, T.-H. Cheng, D. C. Hopkins, V. Amarasinghe, and J. C. W. Ransom, in *32nd International Symposium on Power Semiconductor Devices and ICs (ISPSD)* (IEEE, 2020), p. 242.
[4]P. Sharma, P. Chakrabarty, P. Prajapati, S. Sen, and S. Lodha, Appl. Phys. Lett. **125**(25), 253502 (2024).
[5]D. Chettri, G. Mainali, J. H. Salcedo, M. Kumar, V. Khandelwal, S. Yuvaraja, and X. Li, Appl. Phys. Lett. **125**(20), 202104 (2024).
[6]Y. Guo, Y. Qin, M. Xiao, M. Porter, Q. Song, D. Popa, L. Efthymiou, K. Cheng, I. Kravchenko, L. Shao, H. Wang, F. Udrea, and Y. Zhang, IEEE Electron Device Lett. **46**(4), 556 (2025).
[7]G. Peng, W. Mao, S. Xu, C. Yang, Y. Peng, L. Yu, Y. Zhang, T. Zhang, S. Zhao, C. Zhang, J. Zhang, and Y. Hao, Jpn. J. Appl. Phys. **63**(3), 03SP11 (2024).
[8]Y. Shi, W. Chen, Q. Zhou, and B. Zhang, Superlattices Microstruct. **109**, 414 (2017).
[9]H. Wang, W. Mao, C. Yang, S. Zhao, M. Du, X. Wang, X. Zheng, C. Wang, C. Zhang, J. Zhang, and Y. Hao, Appl. Phys. Express **14**(9), 096502 (2021).
[10]M. T. Alam, S. Mukhopadhyay, M. M. Haque, S. S. Pasayat, and C. Gupta, Appl. Phys. Express **18**(1), 016501 (2025).
[11]G. Baratella, U. Chatterjee, O. Syshchyk, M. Borga, E. Fabris, T. Cosnier, B. Bakeroot, and S. Decoutere, IEEE Trans. Electron Devices **71**(11), 6904 (2024).
[12]B. R. Park, S. W. Han, and H. Y. Cha, IEEE Electron Device Lett. **36**(4), 324 (2015).
[13]P. W. Wheeler, J. Rodriguez, J. C. Clare, L. Empringham, and A. Weinstein, IEEE Trans. Ind. Electron. **49**(2), 276 (2002).
[14]J. Lei, J. Wei, G. Tang, Z. Zhang, Q. Qian, Z. Zheng, M. Hua, and K. J. Chen, IEEE Electron Device Lett. **39**(7), 1003 (2018).
[15]Y. Wu, J. Zhang, S. Zhao, W. Zhang, Y. Zhang, X. Duan, J. Chen, and Y. Hao, IEEE Electron Device Lett. **40**(11), 1724 (2019).
[16]H. Wang, W. Mao, J. Luo, C. Yang, J. Chen, S. Zhao, M. Du, X. Zheng, C. Wang, C. Zhang, J. Zhang, and Y. Hao, IEEE Electron Device Lett. **42**(9), 1264 (2021).
[17]H. Wang, W. Mao, S. Zhao, M. Du, Y. Zhang, X. Zheng, C. Wang, C. Zhang, J. Zhang, and Y. Hao, IEEE J. Electron Devices Soc. **9**, 125 (2021).
[18]Y. K. Lin, S. Noda, C. C. Huang, H. C. Lo, C. H. Wu, Q. H. Luc, P. C. Chang, H. T. Hsu, S. Samukawa, and E. Y. Chang, IEEE Electron Device Lett. **38**(6), 771 (2017).
[19]H. Gao, Y. Gu, Y. Zhang, J. Li, J. Zhou, H. Guo, K. M. Lau, and X. Zou, IEEE Electron Device Lett. **45**(6), 968 (2024).
[20]W. Ye, J. Zhou, H. Gao, H. Guo, Y. Gu, and X. Zou, IEEE Trans. Electron Devices **72**(3), 1035 (2025).
[21]J.-G. Lee, S.-W. Han, B.-R. Park, and H.-Y. Cha, Appl. Phys. Express **7**(1), 014101 (2014).
[22]C. Zhou, W. Chen, E. L. Piner, and K. J. Chen, IEEE Electron Device Lett. **31**(7), 668 (2010).
[23]E. Bahat-Treidel, R. Lossy, J. Wurfl, and G. Trankle, IEEE Electron Device Lett. **30**(9), 901 (2009).
[24]H. Wang, W. Mao, S. Zhao, B. Gao, M. Du, X. Zheng, C. Wang, C. Zhang, J. Zhang, and Y. Hao, Appl. Phys. Lett. **119**(2), 023507 (2021).
[25]C. Summatta, S. Sanmuang, and S. Prainatr, in *15th International Conference on Electrical Engineering/Electronics, Computer, Telecommunications and Information Technology (ECTI-CON)*, 441 (IEEE, 2018).
[26]Z. He, M. Torky, R. Ghandi, C. W. Hitchcock, S. Kennerly, and T. P. Chow, in *36th International Symposium on Power Semiconductor Devices and ICs (ISPSD)* (IEEE, 2024), p. 140.
[27]S. Chowdhury, C. Hitchcock, R. Dahal, I. B. Bhat, and T. P. Chow, in *28th International Symposium on Power Semiconductor Devices and ICs (ISPSD)* (IEEE, 2016), p. 463.

03 November 2025 04:02:20

Published under an exclusive license by AIP Publishing